Global Sizing Optimisation of Permanent Magnet Synchronous Machines Using Dual-Level Response Surface Method based on Mixed-resolution Central Composite Design

Pedram Asef [1*], Ramon Bargallo [1], M. R. Barzegaran [2*]

[1] The Department of Electrical Engineering, Polytechnic University Of Catalonia-BarcelonaTech (UPC), Barcelona, Spain
[2] Phillip M. Drayer Department of Electrical Engineering, Lamar University, 4400 S M L King Jr Pkwy, Beaumont, USA

[*]pedram.asef@upc.edu, barzegaran@lamar.edu

***Abstract*--This paper presents a robust sizing design optimisation of a permanent magnet synchronous generator (PMSG) using three-dimensional finite element analysis (3D FEA). In order to build an optimal parametric model structure, the efficiency of the PMSG is taken as the objective function, and a dual-level response surface methodology (D-RSM) with a window-zoom-in approach for a variable speed range analysis as a robust optimisation technique is employed to find out the optimal design variables of the objective function. The D-RSM using mixed-resolution central composite design (MR-CCD), full factorial design (FFD), central composite design (CCD), and box-behnken design (BBD) is applied to optimise the geometry with very small error. Analysis of variance (ANOVA) and multi-level RSM plots in order to check the adequacy of fit. However, the MR-CCD exceed the range of the boundary in the design region. Hence, a modified MR-CCD has improved the efficiency and proposed the parameter settings to manufacture the wind generator with high-class quality. The validation of the analytical and numerical fashions is successfully achieved through rigorous FEA, and the experimental verifications are perfectly marked the theoretical and significance optimisation design.**

Nomenclature

l_s	Stack length (*mm*)
R_{ri}	Inner radius of the rotor core (*mm*)
R_{ro}	Outer radius of the rotor core (*mm*)
R_{si}	Inner radius of the stator core (*mm*)
R_{so}	Outer radius of the stator core (*mm*)
A_{slot}	Slot area (mm^2)
L_m	Thickness of the magnet (*mm*)
δ_g	Airgap length (*mm*)
S_w	Slot width (*mm*)
P_{arc}	Magnet pole-arc ($^o e$)
S_d	Slot depth (*mm*)
Q_s	The number of slots in stator core
$2P$	Pole number
α_p	Pole-arc/ pole-pitch ratio
χ	Split ratio
SP	Slot/ Pole ratio
M	The number of phases
I_r	Rated current of the power electronic converter
$\Delta\theta$	Winding temperature-rise ($^o C$)
H_k	Permanent magnet coercivity (*A/m*)
H_i	Local field intensity for the *i*th operating point
T_i	Electromagnetic torque of the *i*th operating point
Ω_i	Angular velocity of the *i*th operating point
$i_{d.i}$, $i_{q.I}$	Peak direct and transverse axis currents for *i*th operating point (*A*)
z_1, z_2	Noise variables which are stand for tooth-tip and gap between PMs in MR-CCD (*mm*)

1. Introduction

FOR decades, researchers are employing classic and modern optimisation methodologies in the field of electrical machines and drive systems to improve the efficiency [1-2]. To overcome this issue, various kinds of methods, which emphasise to find out the global optimum only based on a typical torque/speed, or a flux weakening operation point, and many more literature [3]-[6]. However, it is difficult and accordingly rare to reinforce the sizing process optimisation, considering the practical design details of the PMSG and power electronic system for variable-speed applications such as wind generators [7], [8]. The application of response surface methodology (RSM) with different fashions has been recently carried out for electrical machines design optimisations [9]. In another paper [10] presents design optimisation for brushless dc permanent magnet motors for a hard disk driver to reduce cogging torque. This work is a good example of the feasibility of using RSM with typical CCD design function to minimise the cogging torque. But, none other design functions were considered to challenge the accuracy of the fitting model. Also, the lack of experimental verification exists.

In Jolly's paper [11] coupled optimisation design of permanent magnet motors using RSM and genetic algorithms (GAs) has been studied in order to optimize the torque and speed of the machine. However, we believe that a faster and accurate design procedure could be compared if different design functions were defined in the same dimensions. The lack of GA's contribution to the work and also experimental verification can be seen.

A paper by Gao *et al.* [12] presents RSM as an efficient approach to parametric model building and design optimisation. Application of RSM is presented for torque optimisation study in a spindle motor design. The window-zoom-in method has been also studied to improve the torque optimisation performance. This keen study inspired us to employ MR-CCD with zoom-in approach for the optimisation process. To increase the significance of the research, the authors could present the process evaluation before and after

using of zoom-in approach. Moreover, an experimental investigation is ignored.

In reference [13], Yang *et al*. investigates multi-objective optimisation design, and has been proposed a systematic process of a multi-objective sizing design of an axial-flux permanent-magnet motor for electric scooters. The preliminary design has been employed a zero-dimensional (0D) model to determine the number of slots and poles and initial sizes of the motor according to the driving requirements of the scooter. The optimal design process has been used a 1D magnetic circuit model with an effective air-gap distribution function, whereas searching for a set of motor parameters that minimise or maximise motor electromagnetic performance such as back-EMF, torque, torque density and torque ripple. The research was finally verified through the 3D FEA along with experimental verifications.

In this paper, the focus is on developing a global DRSM design optimisation based on the various robust design of experiment (DOE) methods to realize the superior design function for an outer rotor, closed-slot, PMSG with double-layer fractional-slot concentrated winding. The robust design is investigated for a variable-speed range analysis in different subject domains such as numerical analysis model (FEA), and analytical models for the performance evaluation. Therefore, the D-RSM as a multi-level empirical modeling methodology with three-level of window-zoom-in approach is used for the modeling and analysis of problems, in which a response of interest is effected by three controllable variables as magnet thickness, air-gap length, and slot width. The D-RSM affords itself to the design of yields, which can be sensitive to noise variables. There needs to be a rigorous attention to consider the noise variables in the design through modeling the noise and control variables. Afterwards, a combination of settings can be located to the control variables, hence the process output will remain flexible to changes in the noise variables where we proposed modified MR-CCD to improve the efficiency. Moreover, MR-CCD is studied to diminish the experimental runs. Additionally, the FFD, CCD, and BBD as various DOE's methods [14] are taken into account to provide a comparative study in terms of accuracy. Afterwards, the ANOVA calculation will check the adequacy of fit in the design region.

The rest of the paper is organized as follows. In section 2, we provide a definition of the original design, describe the geometry of its rotor and stator and the flux density distribution by FEA. In section 3, we describe optimisation process via the D-RSM using the window-zoom-in approach. In section 4, we present our results and discussion based on the design optimisation to find out the optimal point. In section 5, we have experimental verification to check the successful rate of the optimized model versus the original model, and in section 6, the conclusions is discussed.

2. Original design and problem definition

The objective of this study relies on the PMSG with the outer rotor topology used for a wind turbine, where variable speed range analysis [15] is demanding. The original design parameters can be seen in Table 1. The stator contains 36

Table 1. Original design parameters

Variable	Linear current density fixed: 1.22 *A/ mm*	
l_s	100	*mm*
R_{ri}/ R_{ro}	217/ 230	*mm*
R_{si}/ R_{so}	115/ 209.5	*mm*
δ_g	0.6	*mm*
S_w	15	*mm*
P_{arc}	100	^oe
S_d	50	*mm*
$Q_s/2P$	36/40	
H_k	891×10^3	*A/m*
α_p	0.55	
SP	0.9	
J_{rms}	1.22	*A/ mm*^{2}
m	3	

segmented teeth because of closed slot modulation in order to reduce the amplitude of cogging torque significantly which can be seen in Fig. 1-a. shows a 3D FE model which is coupled with a variable-speed field-circuit PMSG finite element time-stepped model. Fig. 1-b illustrates the design geometrical variables in the model. It should be noted that blue double arrows are representing the uncontrollable variables, and red double arrows stand far controllable variables in this graph. Feeding an uncontrolled three-phase full rectifier load system which is shown in Fig. 1-c as a whole in order to calculate the magnetic flux distribution and corresponding performance via a parameterized model [16].

The global optimisation depends on the PMSG's design, and its electronic system as whole to find out the best possible sizing optimisation in order to maximise the efficiency.

Table I indicates the original design parameters with a fixed current density. Regarding Table II, the three main design variables are defined based on sizing, in which there are controllable variables, and also two uncontrollable variables via a MR-CCD approach which includes under-cut angle of the stator tooth tip δ_{st} changes between $25° \leq z_1 \leq 45°$, and air-gap between PMs ($L_{a\text{-}pm}$) that varies $3° \leq z_2 \leq 5°$. With regarding to the DOE, the BBD, CCD, FFD, and MR-CCD methods will be calculated by 13, 15, 27, 41 runs, respectively.

Fig. 2 shows how the pre-analysis and post-analysis are shown to cater a framework of the study to maximise the efficiency of an acceptable global optimal operation point. Regarding to the flowchart, first, all input data (such as dimensions, constraints, i_{di} (d-axis control current), L_{di} (d-axis inductance), $\tilde{I}$ (moment of inertia), $V_{LL(pk)}$ (peak line to line voltage) of the machine and converter system as a whole analysis loop must be considered, where specifically the converter system is a three-phase full bridge rectifier load that can be seen by Fig. 1-c. Through launching a linked-simulation of FE original model and LUA scripts, the acceptable electromagnetic (EM) performance with reachable operation point of the original PMSG will be stored.

Afterwards, a local sensitivity (LS) analysis finalized the best geometrical variables which can be defined as two groups, controllable, and uncontrollable (noise) variables for the optimisation process. The chosen variables will be evaluated

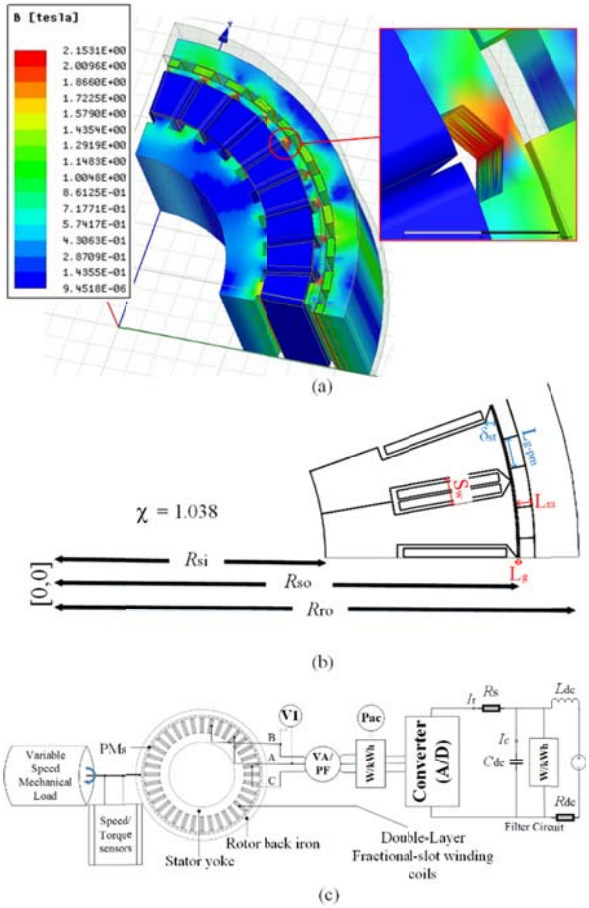

Fig. 1. Schematic of the original 3-D PMSG model at rated speed using FEA, **(a)** magnetic flux density distribution, **(b)** design geometrical variables of the PMSG, **(c)** a coupled three-phase full rectifier load system during test bench

via the ANOVA to validate the adequacy of fit that originated from a number of different methods of DOE such as (the MR-CCD, BBD, CCD, and FFD). Subsequently, the variables under a number of conditional factors for an optimal operation point globalization will be executed to optimize the original PMSG using the D-RSM with the window-zoom-in approach. After that, if only in case the optimized efficiency will be larger than original efficiency, the design optimisation completes via response surface and contour plots. Whereas, the LS analysis must be modified for further performs. Table. II indicates the controllable design variables for all the DOE methods in this study.

3. Dual-level Response Surface Methodology Using Window-Zoom-In

Dual-level response surface methodology (D-RSM) with the window-zoom-in approach is a multi-level collection of mathematical and statistical techniques. The search of the best-fitted operation points through the MR-CCD, BBD, CCD, and FFD functions are calculated. Modeling and analysis of problems, in which a response of interest has affected via a number of variables. The efficiency with a set of defined

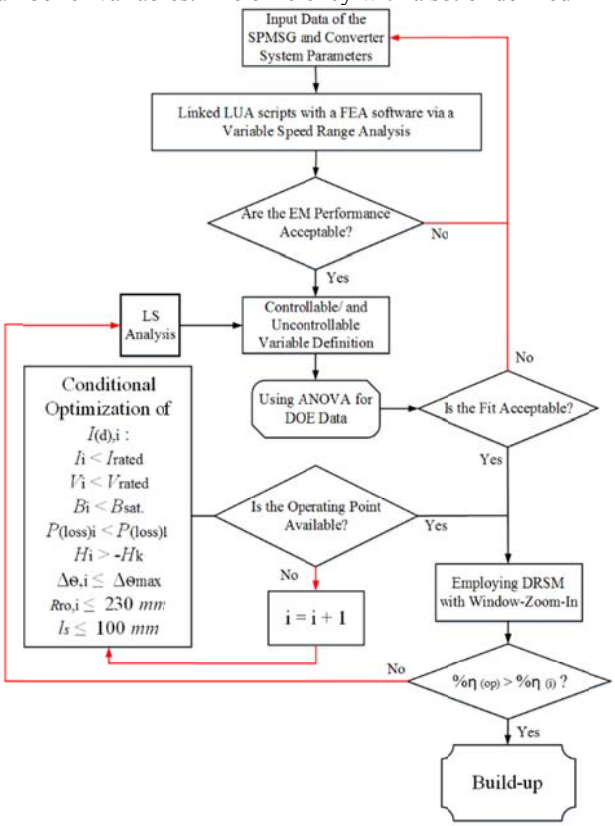

Fig. 2. Flowchart of the proposed objective design global optimisation

constraints optimizes the response in the physical system. The model integrates a curvature at the system to approximate the response [17-18], this study requires the second-order polynomial model given as:

$$y_1 = \beta_0 + \sum_{i=1}^{k}\beta_i x_i + \sum_{i=1}^{k}\beta_{ii} x_i^2 + \sum_{i<j}\sum\beta_{ij} x_i x_j + \epsilon_{ij} \qquad (1)$$

$$x = \begin{bmatrix} x_1 \\ x_2 \\ \vdots \\ x_k \end{bmatrix}, b = \begin{bmatrix} \hat{\beta}_1 \\ \hat{\beta}_2 \\ \vdots \\ \hat{\beta}_k \end{bmatrix}, \& B = \begin{bmatrix} \hat{\beta}_{11} & \hat{\beta}_{12}/2 & \cdots & \hat{\beta}_{1k}/2 \\ \cdots & \hat{\beta}_{22} & \cdots & \hat{\beta}_{2k}/2 \\ \cdots & \cdots & \cdots & \cdots \\ sym. & \cdots & \cdots & \hat{\beta}_{kk} \end{bmatrix} \qquad (2)$$

where x , and b are a *(k×1)* vector of the variables and first-order regression coefficients, respectively. B represents a *(k×k)* symmetrical matrix which includes of pure quadratic coefficients $(\hat{\beta}_{ii})$ in main diagonal elements and for off-diagonal elements, one-half the mixed quadratic coefficients $(\hat{\beta}_{ii}, i \neq j)$. ε is the errors that observed in the response of the first-level window-zoom-in (y_1). ϵ_{ij} integrates any other sources of variability at the experiment through including measurement, variability arising from uncontrollable

variables, and also differences among units [9]. A normalization on variables is always demanded to eliminate the differences of units and suppress generating rounding errors through the next regression analysis. Thus, each design variable (ξ_i) can be coded with a variable (x_i) through its maximum and minimum as follows:

$$x_i = \xi_i - \overline{\xi}_i \big/ \Delta\xi_i \quad (3)$$

where:

$$\overline{\zeta_i} = \left(\xi_{imax} + \xi_{imin}\right)\big/2 \quad \text{and} \quad \Delta\zeta_i = \left(\xi_{imax} - \xi_{min}\right)\big/2 \quad (4)$$

Table 2. Design Controllable Variables

Controllable design treatments		Coded design treatments		
All variables are normalized		-1	0	1
x_1	Magnet thickness (mm), l_m	5	6.5	8
x_2	Air-gap length (mm), l_g	0.5	1.17	2
x_3	Slot width (mm), S_w	8	12	15.5

Table 3. ANOVA of the Fitted Model

Source of Variation	Degree of freedom	Sum of Squares (SS)	Mean Square (MS)
Regression	$p-1$	$SSR = \sum_{i=1}^{n}(\hat{y}_i - \overline{y})^2$	$SSR \ / \ (p-1)$
Residual (Error)	$N-p$	$SSE = \sum_{i=1}^{n}(y_i - \hat{y}_i)^2$	$SSE \ / \ (N-p)$
Total	$N-1$	$SST = \sum_{i=1}^{n}(y_i - \overline{y})^2$	

where ξ_{min}, and ξ_{max} are non-normalized minimum and maximum values of ith variable, respectively. Regarding the framework, the used DOE functions can be sufficiently introduced in the following sections.

3.1 Mixed Resolution Central Composite design (MR-CCD)

The MR-CCD design function is employed to improve the quality of yields and processes by 41 runs (based on [9]). The classic form of the response can be modeled as follows

$$\hat{Y}(x,z) = \beta_0 + x^T\beta + x^T Bx + z^T\gamma + x^T\Delta z + \varepsilon \quad (5)$$

where β_0, β, B, γ, and Δ are coefficients of the controllable variables (x), and uncontrollable variables (z) via a random error (ε). Improved quality results while a higher level of performance has coherently obtained. The best possible performance is obtained by determining the optimal combination of design variables. In this approach, the global optimal operation point should be located using the DOE principles, and also the consistency of performance is performed through carrying out the experimental conditions under the influence of the uncontrollable variables. The MR-CCD function satisfies the needs of problem-solving economically and yield/process design optimisation of the electrical machines owing to the number of runs which is strongly reduced. This advantage brings a higher emphasis on the size and cost of experiments. Moreover, experiment planning and problem formulation based on a modern work disciplines of working as teams can be noted as another main advantage of using this approach [13-14].

3.2 The Full Factorial design (FFD)

This type of design function has known as one of the most expensive experimental design functions due to having the largest size of experiment with considering only controllable treatments which refers three levels of the treatments as low, intermediate, and high (x_1, x_2, x_3) to observe the true response, where the true response η consists an experimental error known as ε_{exp} which is given by the measurement block with a variance (σ^2). In this study, (3^3=27) runs is carried out. In geometrical terms, the observations should be simulated on the vertex of a cube, in the middle of its faces and edges, and at the origin [13-14] [19].

3.3 The Central Composite design (CCD)

The Box-Wilson Central Composite Design function which basically called central composite design (CCD) is studied via many statisticians in the RSM, as well as perhaps is the most popular class of second order designs. The design involves 15 runs which include of eight vertices of the first cube by (±1, ±1, ±1) as cube points, and six star point through (±1.682,0,0), (0, ±1.682,0), and (0, 0, ±1.682), in addition, the origin of the first cube is (0,0,0) [13-14] [19].

3.4 The Box-Behnken design (BBD)

The BBD design function is known as a subset of the FFD, and that is the most economical design only because of its size of experiments in comparison to all other conventional design functions such as FFD, and CCD. It requires 13 runs; hence, the BBD can be comparable to MR-CCD design function only if its error will be as small as the MR-CCD. In terms of complexity, can be called the simplest type of design compared to all other ones. This can be considered while these experiments cannot be realized for practical reasons such as physical constraints issue. Thereafter, the Table III that called ANOVA which can be shown for checking the adequacy of the fit in the design region of each level of optimization. The observation of this table is efficiency of the SPMSG [14][19].

3.5 Optimization Constraints

To consider the local constrained optimization of the d-axis current at each operating point based on [8], [22-23]. The objective evaluation η_i in each operating point with the d-axis current $i_{d,i}$ should be evaluated. To complete the procedure of the optimisation problem, a number of constraints require being defined. Some of the constraints have to be satisfied at each operating point. They can be qualified as instantaneous constraints:

a) Rated current: $\forall i, \sqrt{i_{d,i}^2 + i_{q,i}^2} \le \sqrt{3}.I_r$

b) Rated voltage: $\forall i, \sqrt{v_{d,i}^2 + v_{q,i}^2} \le \sqrt{3}.V_{rated}$

c) EM saturation that needs to be considered in each part of the machine model as $\forall i, B_i(\max) \le B_{sat.}$

d) Demagnetization $\forall i, H_i \ge -H_k$, and lastly

e) The losses evaluation by $\forall i, P_{loss,i} < P_{loss}$

f) Winding temperature-rise $\max(\Delta\theta)_i \le \Delta\theta_{\max}$

where maximum induction level B_i (max) is 1.9 T. At Each operating point of the profile, the parameter is treated independently, and current control is optimized at every operating point to not only minimise the PMSM's drive losses but also satisfy above. A current control strategy (direct and transverse axis current) is used to assist in the extension of the constant speed power range which is validated in [24-26]. Moreover, the minimization of losses based on methods used in [27-28]. This consideration is taken the form of an (i_d,i_q) optimisation to minimise losses at each operating point of the profile respecting other instantaneous constraints (a, b, c, and d). Therefore, $i_{d,i}$ should be optimized, whereas the particular operating point cannot be reached. The mentioned instantaneous constraints c and d are satisfied at each operating point (T_i, Ω_i), where B_{sat} and H_k are subjected to being smaller than 2.0 T and $891*10^3$ $A.m^{-1}$, respectively. The thermal constraint has to be considered with additional attention. The temperature-rise of the hottest point relative to ambient temperature must be calculated accurately by means of a transient thermal model. The maximum value over the entire temperature-rise profile must hence freeze below a threshold value, which means *max* ($\Delta\theta(t)$) ≤ 90 ºC in this paper. The thermal transient analysis is very time consuming, therefore following two definitions are carried out based on thermal time constants (TCs) to allow the simulation run via steady-state thermal analysis:

a) While TCs is large: $\sum_i \Delta\theta_i d_i / \sum_i d_i \le 90(°C)$, and

b) While TCs is small: $Max(\Delta\theta(t)) \le 90\ (°C)$

$\Delta\theta$ is calculated in the winding that corresponds to the temperature-rise between the hottest point of the slot as well as the ambient temperature.

3.6 Model of Machine-Converter System Losses

The copper losses based on the armature resistance per phase (R_s) resolves by the set of geometrical parameters, in addition, the copper resistivity is chosen at the maximum temperature (90ºC). Thus, total copper losses per phase with a slot-filling factor of 0.4 can be calculated as:

$$P_{copper,i} = R_s(i_{d,i}^2 + i_{q,i}^2) \quad (5)$$

Based on the first harmonic hypothesis, the iron losses can be determined as follows:

$$P_{iron,i} = (\frac{2k_H}{\pi})|\Omega_i|\hat{B}_i^2 + \frac{(p.\Omega_i.\hat{B}_i)^2}{2}.\alpha_p \quad (6)$$

where $\hat{B}_i$ is the maximum local flux density for the *i*th operating point. In addition, k_H, and α_p are loss coefficients that are 0.036 A.m/V and 66 A.m/V.s. The total iron losses include iron losses from machine parts (stator yoke, and teeth). The loss densities are considered to be homogeneous in each of these two parts, while through a static analysis, iron losses at the rotor yoke are nearly zero in the 1st harmonic.

Dual-level optimization process mover is based on the window-zoom-in approach is defined for all design functions (MR-CCD, FFD, CCD, and BBD). Each window defines the range of controllable and uncontrollable variables which should be scanned through a response surface of the prototype with an acceptable operation point in the boundary. Fig. 3 represents that how the movement of each window will approach the global optimal operation point using steepest gradient between two controllable variables. The black curves find out the 1st –level optimal operation point of the original prototype in the boundary and blue curves ended up with the 2nd –level optimal operation point with a new range definition.

4. Results and Discussion

In this section, how the design optimisation with the purpose of finding a global optimal operation point for efficiency maximization will be discussed via a multi-

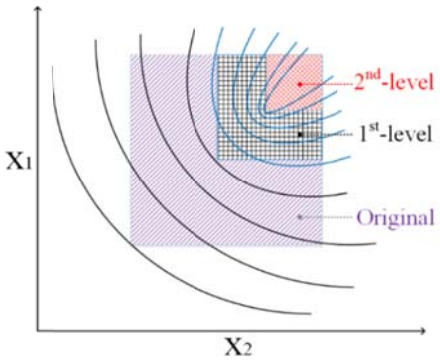

Fig. 3. Dual-level windows moving and zoom-in framework

disciplinary study, in which the results of each optimisation process are presented.

Fig. 3 demonstrates how the window mover works to reach the best optimal operation point from the original window to the final window that is 2nd –level window.

Regarding the eq. (1), the best optimal operation point through presented coefficients (in Table IV) using FFD is reachable in the boundary. However, the focus is obtaining the best optimal operation point through MR-CCD with reaching a higher number of the experiment (41) in comparison to the FFD with 27 experiments. Eventually, the above ANOVA using un-replicated factorials, uncontrollable variables z_1, and z_2 exceed the range of the boundary. Therefore, the true optimal point cannot be comparable with other used approaches. For further analysis, the boundary should be moved to the lower boundary ($15° \le z_{1'} \le 35°$, and $2° \le z_{2'} \le 4°$) of the original range on the MR-CCD. The variables regions are readjusted in Table V. Regarding this fact, the modified MR-CCD can be resulted as shown in Table VI, and compared to the initial MR-CCD. Although, there is a small improvement on the R^2 using modified-MR-CCD with (0.02) and less error in comparison to the FFD in the same range due

to the different boundary adjustment on the uncontrollable variables. Also, much more complexity to use MR-CCD in order to complete with an acceptable outcome with the same boundary. The FFD approach is fairly preferred for a further stage of design optimisation. Fig. 4 presents that how fitted-model has been improved in Table V to decrease the error from 0.15 to less than 0.0015 in average. According to the fitted-model on the RSM, the prediction of the objective can be compared to FEA validation to check the error which is suppressed by the window-zoom-in approach. Regarding the prediction of fitted-model, a very small is strongly considered in the D-RSM. The finalized fitted second-order regression model can be given as:

$$\hat{Y}(x_1,x_2,x_3) = 96.345 + 0.054x_1 - 0.029x_2 + 0.269x_3 + 2.358\times10^{-3}x_1.x_2 + 3.583\times10^{-4}x_1.x_3 + 3.017\times10^{-3}x_2.x_3 - 4.083\times10^{-3}x_1^2 - 7.667\times10^{-4}x_2^2 - 0.03x_3^2 \quad (6)$$

The first and second-levels of RSM using FFD with the calculated second-order regression model can be reported via Table IV based on equation (1), where average error is:

$$Error_{ave} = \frac{1}{27}\sum_{i=1}^{27}\left|\frac{y_i - \hat{y}_i}{y_i}\right| \quad (7)$$

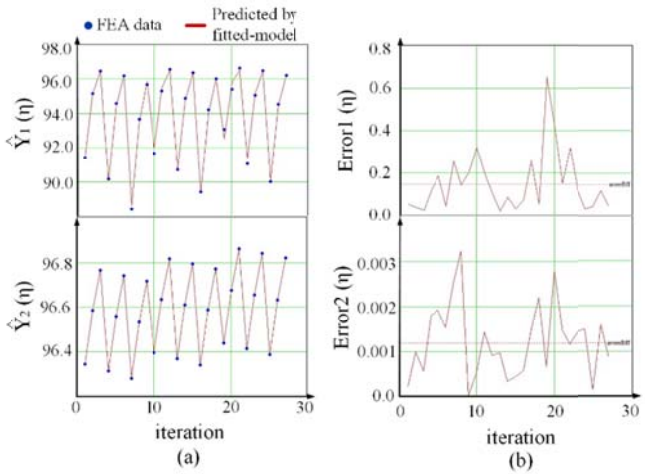

Fig. 4. Predicted efficiency by the fitted-model via **(a)** the 1st -level and 2nd –level fitted-models ($\hat{Y}_1(\eta)$, and $\hat{Y}_2(\eta)$), with **(b)** their corresponding errors for each level

The fitted regression model is checked via *F-value* statistic to ascertain the validity under the null hypothesis as:

$$F = SSR(a-1)^{-1}/SSE(N-a)^{-1} \quad (8)$$

where *SSR*, *SSE*, and *a* are random regression sum of squares, random residual sum of squares, and the number of terms at the fitted-model, respectively. R^2 is an important statistic to express the proportion of the variation of the y_i by fitted-model and FEA data for mean of $\bar{y}$ as:

$$R^2 = SSR(SST)^{-1} \quad (9)$$

For checking the adequacy of fit in the design region, the ANOVA is employed through developing a linear statistical model as:

$$y_{ij} = \mu + \tau_i + \epsilon_{ij} \begin{cases} i = 1,2,\ldots,a \\ j = 1,2,\ldots,n \end{cases} \quad (10)$$

ANOVA using un-replicated factorials, in which the total and error refer to regression, and residual, respectively. Based on the Table V, R^2-*value* using MR-CCD, FFD, CCD, and BBD are 0.9998, 0.9992, 0.9987, and 0.9982, respectively. Among all design function, the efficieny of MR-CCD was increased to the maximum value of 99.98% during the rated-speed-operation.

Fig. 5 comprehensively presents a variable-speed-range functional objective as the efficiency. Based on the framework, the optimal efficiency through a global sizing optimisation was drawn into the true responses, in where, Fig. 5-a indicates the response to the controllable variables (x_1, x_2) at the lowest shaft rotation of 15 rpm maximum reachable efficiency of %90.15. Fig. 5-a illustrates the 99.93% of the total variation in efficiency, in which the MR-CCD has minimum error of 0.28% in the same boundary range, whereas BBD carries the maximum value of error with 0.97%. Thus, ANOVA is

Table 4. Coefficients of Second-order Regression Model at 1st-level and 2nd-level RSM

Coefficients	First-level	Second-level
β_0	91.382	96.345
β_1	0.568	0.054
β_2	-1.247	-0.029
β_3	5.115	0.269
β_4	0.075	2.358×10^-3
β_5	-0.265	3.583×10^-4
β_6	0.548	3.017×10^-3
β_7	-5.833×10^-4	-4.083×10^-3
β_8	-0.063	-7.667×10^-4
β_9	-1.296	-0.03

Table 5. ANOVA Using Different DOE's Methods with 5% level

Method	Source	Sum of Squares	DF	Mean square	*F*	R^2 (%)
MR-CCD	x_1	0.228	-	0.228	0.288	-
	x_2	69.06	-	69.06	50.54	-
	x_3	0.53	-	0.53	0.039	-
	Total	80.56	40	-	-	99.98
	Error	0.28%	11	1.544	-	-
FFD	x_1	0.399	-	0.399	0.297	-
	x_2	71.059	-	71.059	52.905	-
	x_3	0.068	-	0.068	0.051	-
	Total	71.526	7	-	-	99.92
	Error	0.53%	4	1.343	-	-
CCD	x_1	0.466	-	0.466	0.381	-
	x_2	81.005	-	81.005	53.37	-
	x_3	0.789	-	0.789	0.0831	-
	Total	82.26	8	-	-	99.87
	Error	0.6%	4	1.778	-	-
BBD	x_1	0.77	-	0.77	0.799	-
	x_2	84.92	-	84.92	0.1	-
	x_3	1.51	-	1.51	$6.98*10^{-3}$	-

	Total	86,2	12	-	-	99.82
	Error	0.97%	5	2.095	-	-

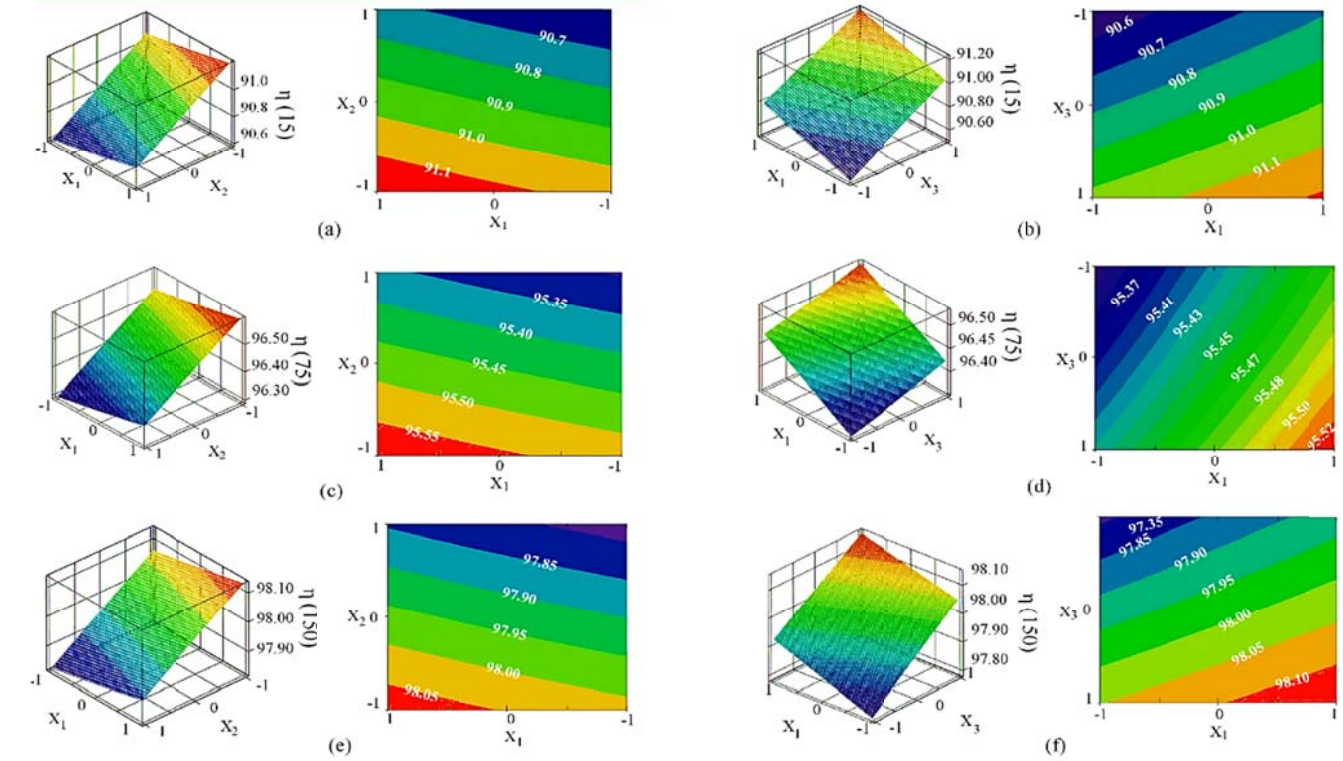

Fig. 5. Surface and counter plots of D-RSM results for variable-speed-range-objective from minimum speed of 15 up to the rated speed 150 (rpm), **(a)** l_m versus l_g @15 (rpm), **(b)** l_m versus S_w @15 (rpm), **(c)** l_m versus l_g @75 (rpm), **(d)** l_m versus S_w @75 (rpm), **(e)** l_m versus l_g @150 (rpm), and **(f)** l_m versus S_w @150 (rpm)

Table 6. ANOVA Using Mixed-Resolution-CCD

Method	Source	Sum of Squares	DF	Mean square	*F*	R^2 (%)
MR-CCD	x_1	0.228	-	0.228	0.288	-
	x_2	69.06	-	69.06	50.54	-
	x_3	0.53	-	0.53	0.039	-
	Total	80.56	40	-	-	99.96
	Error	0.574%	11	1.544	-	-
Modified-MR-CCD	x_1	0.393	-	0.399	0.297	-
	x_2	71	-	71.059	52.905	-
	x_3	0.066	-	0.068	0.051	-
	Total	71.459	40	-	-	99.98
	Error	0.457%	11	1.343	-	-

performed to examine how good the fitted-model can be able to predict the response at any observation points, and for this target, *SST*, *F-value*, and R^2-*value* which belongs to the variations of the response were calculated. Fig. 5-b represents controllable variables of (x_1, x_3), in which maximises the efficiency of %91.2. The response for the controllable variables (x_1, x_2) with a speed raise to 75 rpm is shown in Fig. 5-c, when a larger efficiency obtained through controllable variables of (x_1, x_3) as presented in Fig. 5-d to analyse the effect of each controllable variable on the efficiency. Regarding the knowledge of the operation environment, the generator is compulsory to provide the best performance and also efficient at the rated speed which is 150 rpm. Fig. 5-e-f represents that the response based on the defined variables is significant with maximum efficiency of 98.13. Therefore, the fitted-model is successfully performed over the variable-speed-range analysis.

The optimisation process to achieve the global optimal operation point for the variable-speed-range application can be reported through Table VII, where the optimal operation point deals with *dq*-plane inductances, and also efficiency maximization, in which the output power is considered fixed in this study. The optimized efficiency is reported in Table VII at the rated speed of 150 rpm, the maximum reachable efficiency of %98.13 was reached.

5. Experimental Verification

The manufactured generator (cf., Fig. 6) is applied for the small power generation through wind energy along the coast of Barcelona city in Spain. The back-EMF in comparison to original and optimized models can be seen in Fig. 7-a, where a considerable accuracy between the optimized generator and measured values presents a great fitness for the optimisation design. The employed equipment to measure the optimal PMSG under test is fed via a variable speed frequency converter known as ABB ACsS600 and loaded through a DC machine. The electrical output power is measured using a power analyser known as Yokogawa PZ4000 with 1%

accuracy. The temperature is registered in twenty points through Pt-100 temperature sensors. The manufactured PMSG is shown in Fig. 6 via segmented stator-teeth core for improving slot fill factor, simpler winding, and providing closed-slot topology which is illustrated in Fig. 6-a-b. The optimized thickness of the magnets were manufactured with 7.8 mm, shown in Fig. 6-c. The efficiency improvement as a main objective of the project is

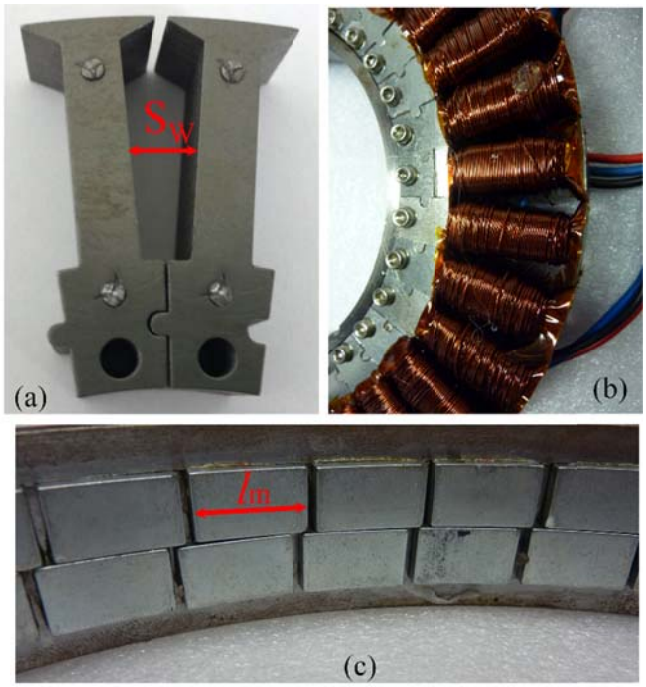

Fig. 6. Manufactured optimized generator, **(a)** the tooth, **(b)** mounted stator core, and **(c)** permanent magnets on the rotor

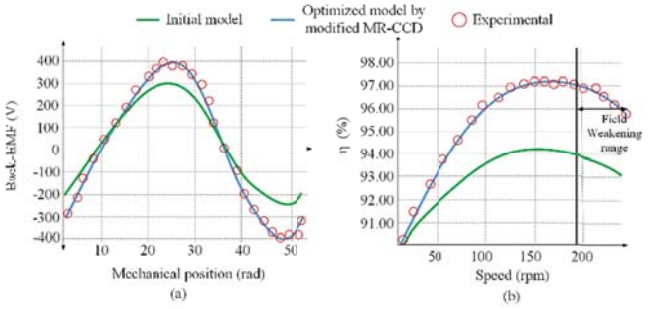

Fig. 7. Comparison of performance evaluation among original model, optimised model along with experimental verification, **(a)** back-EMF comparison, **(b)** efficiency improvement

improved from 94.23% to 97.13%, which is verified via experimental investigation that can be drawn in Fig. 7-b.

Lastly, the infrared thermal imaging is done by FLIR E60bx–SERIES, shown in Fig. 8, that has thermal sensitivity of <0.045°C, and accuracy of ±2%. Based on the applied thermal constraint of 90°C, the temperature distribution at the optimised model was recorded under 65°C.

Table 7. Optimisation Results And Verification

Parameters at rated speed	Pre-optimisation	Post-optimisation	FEA verification
L_d (mH)	468.26	470.76	470.88
L_q (mH)	468. 21	471	470.96
E_p (V)	315	414	428
λ_m (mVs)	1691.88	1720.43	1719.72
P_o (W)	455.75	460.84	469.44
P_{copper} (W)	46.8	33.5	34.0
P_{iron} (W)	226.6	206.5	207.3
η (%)	94.23	97.13	97.10

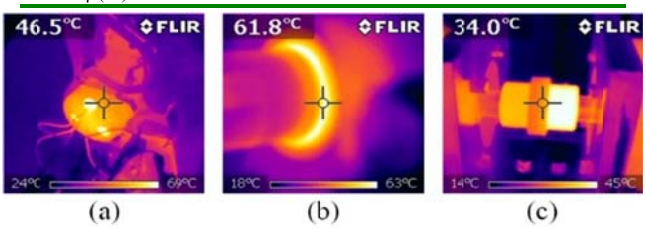

Fig. 8. Use of infrared thermal imaging measurement on the test bench at rated speed, **(a)** the stator core, **(b)** the rotor core, and **(c)** the housing

6. Conclusion

A global design optimisation framework (cf., Fig. 3) proposed, in which 3-D FEA and D-RSM are used for a machine-converter-system design optimisation with a strong coupling between the machine and the power electronic converter. The D-RSM with moving least-squares approach using various design functions such as MR-CCD, FFD, CCD, and BBD with a number of constraints optimisation as a function of $i_{d,i}$, the values of currents $i_{d\ ,i}$ at each operating point have to constitute significantly optimisation parameters to the same extent as machine-converter-system sizing parameters. The window-zoom-in approach is carried out as a mover from the original plane to the 2nd–level plane to find out the global optimal operation point. A set of considerations and assumptions are considered. We found that the modified-MR-CCD originates from a different set of the boundary to complete the use of MR-CCD, yet, the adequacy of fit in the design region using FFD is significant and cost-efficient. The influence of the sizing optimisation methodology absolutely satisfies the objective improvement. The outcome of the sizing optimisation, in which the pre-optimisation and post-optimisation results are compared, and verified by FEA with an error less than 0.5%. Finally, the experimental verifications are proved the sizing design optimisation through a high-quality prestige. Moreover, the influence of flux weakening on the model can be highly recommended for further study.

7. References

[1] R. J. Wai, C. Y. Lin, and Y. R. Chang "Novel maximum-power-extraction algorithm for PMSG wind generation system," *IET Electric Power Applications*, DOI: doi:10.1049/iet-epa:20050514, vol. 1, pp. 275–283, 2007.

[2] A. Mahmoudi, S. Kahourzade, N. A. Rahim, H. Wooi Ping, and M. N. Uddin, "Design and prototyping of an optimised axial-flux permanent-magnet synchronous machine," *IET Electric Power Applications*, DOI: 10.1049/iet-epa.2012.0377, vol. 7, pp. 338–349, 2013.

[3] N. Boules, "Design optimization of permanent magnet dc motors," *IEEE Trans. Ind. Appl.*, vol. 26, no. 4, pp. 786–792, Jul. 1990.

[4] G. Slemon and X. Liu, "Modeling and design optimization of permanent magnet motors," *Elect. Power Compon. Syst.*, v.20, n.2, pp.71–92, 1992.

[5] J.-L. Shi, T.-H. Liu and S.-H. Yang, "Nonlinear-controller design for an interior-permanent-magnet synchronous motor including field-

weakening operation," *IET Electric Power Applications*, DOI: 10.1049/iet-epa:20060151 vol. 1, no. 1, pp. 119–126, 2007.

[6] K. Laskaris and A. G. Kladas, "Internal permanent magnet motor design for electric vehicle drive," *IEEE Trans. Ind. Elctrns.*, v. 57, n. 1, pp. 138–145, Jan. 2010.

[7] D. Dorrell, *et al*., "A review of the design issues and techniques for radial-flux brushless surface and internal rare-earth permanent magnet motors," *IEEE Trans. Ind. Electron.*, v. 58, n. 9, pp. 3741–3757, 2011.

[8] J. Aubry, *et al*., "Sizing Optimization Methodology of a Surface Permanent Magnet Machine-Converter System Over a Torque-Speed Operating Profile: Application to a Wave Energy Converter," *IEEE Trans. Ind. Elctrns.*, v. 59, n. 5, pp. 2116–2124, 2012.

[9] H. Terrab, and A. Kara, "Parameters design optimization of 230 kV corona ring based on electric field analysis and response surface methodology," *Electric Power Systems Research*, DOI: http://dx.doi.org/10.1016/j.epsr.2017.06.002, pp. 1–7, 2017.

[10] J. T. Li, *et al*., "Design Optimization for Cogging Torque Minimization Using Response Surface Methodology," *IEEE Trans. Magn.*, vol. 40, no. 2, pp. 1176–1179, March. 2004.

[11] L. Jolly, *et al*., "Design Optimization of Permanent Magnet Motors Using Response Surface Methodologyand Genetic Algorithms," *IEEE Tran. Magn*, V. 41, N. 10, Oct 2005, pp.3928-3930.

[12] X. K. Gao, *et al*., "Robust design for torque optimization using response surface methodology," *IEEE Trans. Magn*, VOL. 38, NO. 2, pp.1141-1144, 2002.

[13] Yee-Pien Yang, Chung-Han Lee, and Po-Chang Hung, "Multi-objective optimal design of an axial-flux permanent-magnet wheel motor for electric scooters," *IET Electric Power Applications*, DOI: 10.1049/iet-epa.2013.0026. Vol. 8, No. 1, pp. 1-12, 2014.

[14] D. C. Montgomery, "Design and Analysis of Experiments" John Wiley & Sons Singapore, pp.65-544, 2013.

[15] H-Woo Kim, S-Soo Kim, and H-Sang Ko, "Modeling and control of PMSG-based variable-speed wind turbine," *Electric Power Systems Research*, DOI: 10.1016/j.epsr.2009.08.003, vol. 80, pp. 46–52, 2010.

[16] E.G. Shehata, "A comparative study of current control schemes for a direct-driven PMSG wind energy generation system," *Electric Power Systems Research*, DOI: http://dx.doi.org/10.1016/j.epsr.2016.10.039, vol. 143, pp. 197–205, 2017.

[17] W. Zhao, and Z. Qiu, "An efficient response surface method and its application to structural reliability and reliability-based optimization," *Finite Elements in Analysis and Design*, DOI: https://doi.org/10.1016/j.finel.2012.12.004, vol. 67, pp. 34–42, 2013.

[18] K-Sun Yoo, Y-S. Eom, J-Y. Park, M-G. Lm, and S-Y. Han "Reliability-based topology optimization using successive standard response surface method," *Finite Elements in Analysis and Design*, DOI: https://doi.org/10.1016/j.finel.2011.02.015, vol. 47, pp. 843–849, 2011.

[19] Sung-Ho Lee, *et al*., "Multiobjective Optimization Design of Small-Scale Wind Power Generator with Outer Rotor Based on Box–Behnken Design," IEEE Trans. on Applied Superconductivity, VOL. 26, NO. 4, JUNE 2016, pp. 1-5, 2016.

[20] W. Li, and C. Su, "Modeling and Optimization of Acid Chrome Dark Blue Degradation by Fenton using Box-Behnken Response Surface Methodology," *IEEE-MACE*, pp. 7463-7465, 2011.

[21] T. M. Jahns, "Flux-weakening regime operation of an interior permanent magnet synchronous motor drive," *IEEE Trans. Ind. Appl*., vol. IA-23, no. 4, pp. 681–689, Jul. 1987.

[22] S. Morimoto, *et al*., "Expansion of operating limits for permanent magnet motor by current vector control considering inverter capacity," *IEEE Trans. Ind. Appl*., vol. 26, no. 5, pp. 866–871, Sep. 1990.

[23] S. Morimoto, *et al*., "Expansion of operating limits for permanent magnet motor by current vector control considering inverter capacity," *IEEE Trans. Ind. Appl.*, vol. 26, no. 5, pp. 866–871, Sep. 1990.

[24] C. Mademlis, J. Xypteras, and N. Margaris, "Loss minimization in surface permanent-magnet synchronous motor drives," *IEEE Trans. Ind. Electron.*, vol. 47, no. 1, pp. 115–122, Feb. 2000.

[25] J-Tao Zhang, H. Zhu, S-Q. Zhou, and C-S. Zhao, "Optimal design of a rod shape ultrasonic motor using sequential quadratic programming and finite element method," *Finite Elements in Analysis and Design*, DOI: https://doi.org/10.1016/j.finel.2012.04.011, vol. 59, pp. 11–17, 2012.

[26] Y. S. Chen, Y. D. Cheng. J.J. Liao, and C. C. Chiou, "Development of a finite element solution module for the analysis of the dynamic behavior and balancing effects of an induction motor system," *Finite Elements in Analysis and Design*, DOI: https://doi.org/10.1016/j.finel.2008.01.006, vol. 44, Issue. 8, pp. 483–492, 2008.

[27] C. Cavallaro, A. O. DiTommaso, R. Miceli, A. Raciti, G. Galluzzo, and M. Trapanese, "Efficiency enhancement of permanent-magnet synchronous motor drives by online loss minimization approaches," *IEEE Trans. Ind. Electron.*, vol. 52, no. 4, pp. 1154–1160, Aug. 2005.

[28] L. Chedot, G. Friedrich, J.-M. Biedinger, and P. Macret, "Integrated starter generator: The need for an optimal design and control approach. Application to a permanent magnet machine," *IEEE Trans. Ind. Appl.*, vol. 43, no. 2, pp. 552–559, Mar. 2007.